

## Constraining the nature of the 18 min periodic radio transient GLEAM-X J162759.5-523504.3 via multi-wavelength observations and magneto-thermal simulations

N. REA <sup>1,2</sup> F. COTI ZELATI <sup>1,2</sup> C. DEHMAN <sup>1,2</sup> N. HURLEY-WALKER <sup>3</sup> D. DE MARTINO <sup>4</sup> A. BAHRAMIAN <sup>3</sup>  
D. A. H. BUCKLEY <sup>5,6</sup> J. BRINK <sup>5,6</sup> A. KAWKA <sup>3</sup> J. A. PONS <sup>7</sup> D. VIGANÒ <sup>1,2</sup> V. GRABER <sup>1,2</sup> M. RONCHI <sup>1,2</sup>  
C. PARDO ARAUJO,<sup>1,2</sup> A. BORGHESE <sup>1,2</sup> AND E. PARENT <sup>1,2</sup>

<sup>1</sup>*Institute of Space Sciences (ICE), CSIC, Campus UAB, Carrer de Can Magrans s/n, E-08193, Barcelona, Spain*

<sup>2</sup>*Institut d'Estudis Espacials de Catalunya (IEEC), Carrer Gran Capità 2-4, E-08034 Barcelona, Spain*

<sup>3</sup>*International Centre for Radio Astronomy Research, Curtin University, Kent St, Bentley WA 6102, Australia*

<sup>4</sup>*INAF-Osservatorio Astronomico di Capodimonte, Salita Moiariello 16, I-80131 Napoli, Italy*

<sup>5</sup>*South African Astronomical Observatory, PO Box 9, Observatory Road, Observatory 7935, Cape Town, South Africa*

<sup>6</sup>*Department of Astronomy, University of Cape Town, Private Bag X3, Rondebosch 7701, South Africa*

<sup>7</sup>*Departament de Física Aplicada, Universitat d'Alacant, 03690 Alicante, Spain*

Submitted to ApJ

### ABSTRACT

We observed the periodic radio transient GLEAM-X J162759.5-523504.3 (GLEAM-X J1627) using the *Chandra X-ray Observatory* for about 30 ks on January 22–23, 2022, simultaneously with radio observations from MWA, MeerKAT and ATCA. Its radio emission and 18 min periodicity led the source to be tentatively interpreted as an extreme magnetar or a peculiar highly magnetic white dwarf. The source was not detected in the 0.3–8 keV energy range with a  $3\sigma$  upper-limit on the count rate of  $3 \times 10^{-4}$  counts  $s^{-1}$ . No radio emission was detected during our X-ray observations either. Furthermore, we studied the field around GLEAM-X J1627 using archival ESO and DECam data, as well as recent SALT observations. Many sources are present close to the position of GLEAM-X J1627, but only two within the  $2''$  radio position uncertainty. Depending on the assumed spectral distribution, the upper limits converted to an X-ray luminosity of  $L_X < 6.5 \times 10^{29}$  erg  $s^{-1}$  for a blackbody with temperature  $kT = 0.3$  keV, or  $L_X < 9 \times 10^{29}$  erg  $s^{-1}$  for a power-law with photon index  $\Gamma = 2$  (assuming a 1.3 kpc distance). Furthermore, we performed magneto-thermal simulations for neutron stars considering crust- and core-dominated field configurations. Based on our multi-band limits, we conclude that: i) in the magnetar scenario, the X-ray upper limits suggest that GLEAM-X J1627 should be older than  $\sim 1$  Myr, unless it has a core-dominated magnetic field or has experienced fast-cooling; ii) in the white dwarf scenario, we can rule out most binary systems, a hot sub-dwarf and a hot magnetic isolated white dwarf ( $T \gtrsim 10,000$  K), while a cold isolated white dwarf is still compatible with our limits.

*Keywords:* stars: magnetars – stars: neutron - pulsars: general – pulsars: individual (GLEAM-X J162759.5-523504.3) – radio continuum: transients

### 1. INTRODUCTION

The spin-period ( $P$ ) evolution of a pulsar is driven by the combination of several factors: the presence of accretion during its lifetime either from supernova fall-back or a companion star, the dissipation of the magnetic field over time due to currents inside and outside the neutron star crust, the consumption of rotational energy via dipolar spin-down emission, occasional glitch events, etc. (Lyne et al. 1985; Manch-

ester & Taylor 1977). The population of rotational-powered radio pulsars has been observed to have spin periods in the range  $P \sim 0.0014 - 12$  s (Manchester et al. 2005). The majority of the observed population clusters around  $P \sim 1$  s, with the extremes being populated on the fast side by rapidly spinning recycled millisecond pulsars and on the slow side by magnetars. The spin distribution of classical magnetars (Kaspi & Beloborodov 2017; Esposito et al. 2021) ranges between  $\sim 1.4$  s for Swift J1818.0–1607, a young radio magnetar recently discovered during an outburst (Esposito et al. 2020), and  $\sim 12$  s for the bright hard X-ray emitting magnetar 1E 1841–045 (Vasisht & Gotthelf 1997). However, the discovery of magnetar-like activity from the high magnetic field,

**Table 1.** X-ray and Radio observations.

Instrument	Start Time (UTC) (YYYY Mmm DD hh:mm:ss)	End Time (UTC) (YYYY Mmm DD hh:mm:ss)	Exposure <sup>a</sup> (ks)	Obs. ID	Mode <sup>b</sup>
<i>Chandra</i>	2022 Jan 22 20:50:23	2022 Jan 23 03:04:34	19.82	26228	TE VF (3.041 s)
<i>Chandra</i>	2022 Jan 23 06:03:38	2022 Jan 23 09:25:25	9.98	26282	TE VF (3.141 s)
Instrument	Start Time (UTC) (YYYY Mmm DD hh:mm:ss)	End Time (UTC) (YYYY Mmm DD hh:mm:ss)	Integration time <sup>c</sup> (minutes)	Observing Band (GHz)	3 $\sigma$ limit ( $\mu$ Jy beam <sup>-1</sup> )
MWA	2022 Jan 21 23:45:58	2022 Jan 22 01:24:38	111	0.17 – 0.2	–
MWA	2022 Jan 22 23:45:58	2022 Jan 23 01:24:38	111	0.17 – 0.2	5000
MeerKAT	2022 Jan 23 03:32:49	2022 Jan 23 05:12:48	70	0.58 – 1.1	84
ATCA	2022 Jan 22 15:00:18	2022 Jan 22 19:41:42	252	4 – 6	72
ATCA	2022 Jan 22 15:00:18	2022 Jan 22 19:41:42	252	8 – 10	60

<sup>a</sup> Deadtime corrected on-source time.

<sup>b</sup> TE: Timed Exposure, VF: Very Faint telemetry format; the temporal resolution is given in parentheses.

<sup>c</sup> On-source only; not including time spent on calibrators.

rotation-powered pulsars PSR J1119–6127 ( $P \sim 0.11$  s; Göğüş et al. 2016) and PSR J1846–0258 ( $P \sim 0.3$  s; Gavriil et al. 2008), as well as from 1E 161348-5055 at the center of the supernova remnant RCW103 ( $P \sim 6.67$  hr; Rea et al. 2016; D’Ai et al. 2016), has enlarged the historical magnetar spin-period range. Furthermore, a few rotational-powered radio pulsars have been recently discovered with periods larger than the classical magnetar range: PSR J1903+0433 ( $P \sim 14.1$  s; Han et al. 2021), PSR J0250+5854 ( $P \sim 23.5$  s; Tan et al. 2018) and PSR J0901–4046 ( $P \sim 76$  s; Caleb et al. 2022) (see also Fig. 1).

On the other hand, the spin periods of magnetic white dwarfs range between  $\sim 0.019$ – $10^4$  hr (Brinkworth et al. 2013; Ferrario et al. 2020; Kilic et al. 2021). Magnetic white dwarfs have been observed both isolated (about 600 detected thus far) and in interacting binaries (about 200 detected), with magnetic fields reaching  $\sim 10^9$  G. Periodic radio and optical emission has only been detected from the binary star AR Sco at the beat frequency between its spin and orbital periods (Marsh et al. 2016). The incoherent nature of the pulsed radio emission from AR Sco has pointed towards models involving particle acceleration due to the interaction between the two stars rather than canonical pulsar radio emission (Geng et al. 2016).

A peculiar radio transient with a periodicity of  $\sim 1091$  s (GLEAM-XJ162759.5-523504.3; GLEAM-XJ1627 hereafter) was discovered in archival data taken by the Murchison Widefield Array (MWA; Tingay et al. 2013; Wayth et al. 2018). This source was found to be active during January–March 2018 with 5–40 Jy bright radio pulses lasting about 10–30 s and repeating with an 18-min periodicity (Hurley-Walker et al. 2022). The bright pulses have a linear polarization degree of  $88 \pm 1\%$  and a dispersion measure  $DM = 57 \pm 1$  pc cm<sup>-3</sup>, the latter resulting in a distance of  $1.3 \pm 0.5$  kpc according to the Galactic electron-density model by Yao et al. (2017). The observed radio luminosity and emis-

sion timescales pointed to a coherent emission process. On the one hand, the long spin period would be explained by a rotating magnetic white dwarf emitting as a pulsar-like dipole. On the other hand, the source radio properties resembled those of radio magnetars. In any of the above-mentioned cases, the nature of this source would be quite extreme within these source classes (Hurley-Walker et al. 2022). In this work we report on X-ray observations of GLEAM-XJ1627 performed with the *Chandra X-ray Observatory* on January 22–23, 2022 (§2.1) and simultaneous radio observations using MWA, MeerKAT, and the Australia Telescope Compact Array (ATCA; §2.2). We also report on optical and near infrared (nIR) data sets collected in ESO public survey projects and in the DECAM Plane Survey, as well as optical data acquired in recent SALT observations (§2.3). We use these observations to constrain the nature of this periodic radio transient both in the neutron star and white dwarf scenarios. We report the results in §3 and discuss them in §4. Conclusions follow in §5.

## 2. OBSERVATIONS AND DATA ANALYSIS

### 2.1. X-ray observations: *Chandra*

The *Chandra X-ray Observatory* observed GLEAM-XJ1627 twice using the Advanced CCD Imaging Spectrometer (ACIS; Garmire et al. 2003) instrument, from 2022 January 22 at 20:51:32 to January 23 at 03:05:43 TT (ObsID: 26228), and then again on 2022 January 23 from 06:04:47 to 09:26:34 TT (ObsID: 26282). All observations were performed in timed exposure imaging mode with VERY FAINT (VF) telemetry format. The source was positioned on the back-illuminated ACIS-S3 CCD at the nominal target position (R.A. =  $16^{\text{h}}27^{\text{m}}59^{\text{s}}.5$ , decl. =  $-52^{\circ}35'04''.3$ ; J2000.0; uncertainty of  $2''$ ; Hurley-Walker et al. 2022).

Standard processing of the data was performed by the *Chandra X-ray Center* to Level 1 and Level 2 (processing software DS 10.10.2.1). The data were reprocessed using the

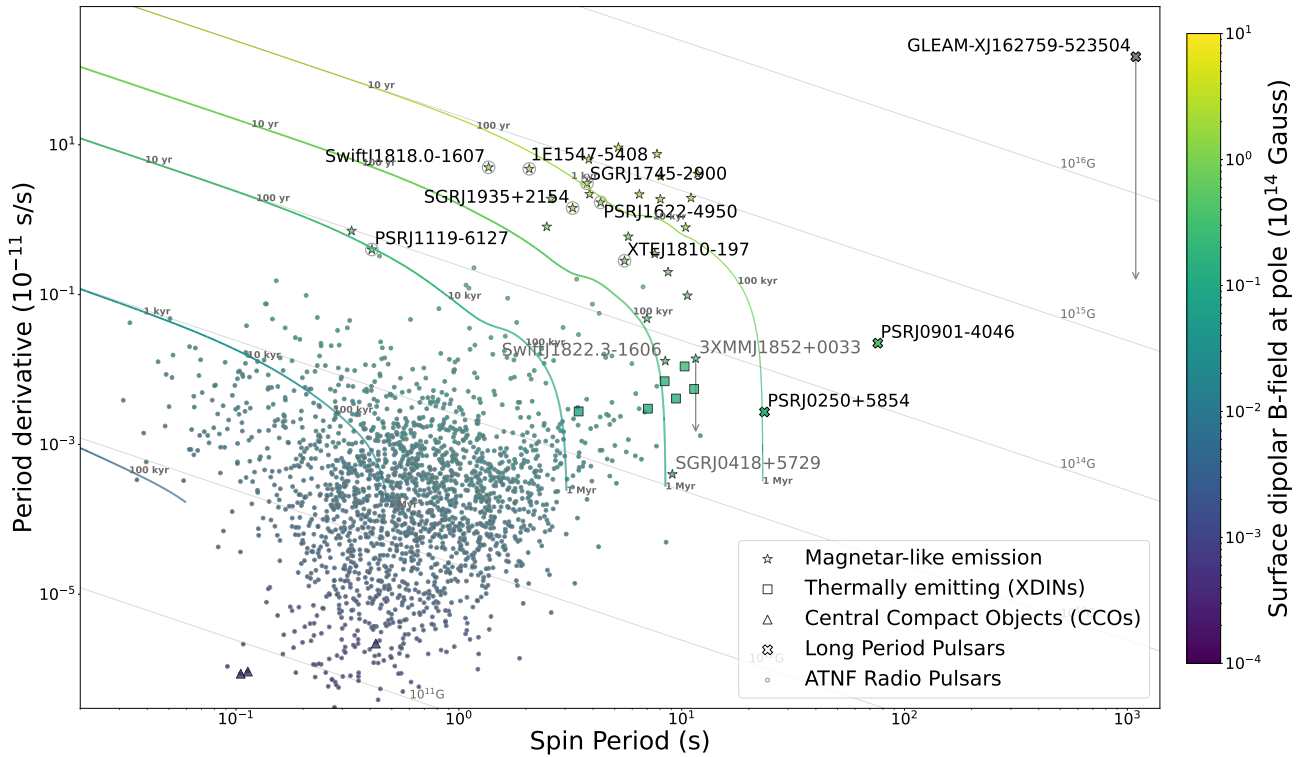


**Figure 1.**  $P-\dot{P}$  diagram for different neutron star classes. The names are shown for radio-magnetars (also displayed with a gray circle), low-field magnetars, and long-period pulsars (including GLEAM-X J1627). Light gray lines correspond to constant magnetic fields, while the colored curves assumed magnetic field decay in the crust (see §4 for details). Colors refer to the surface dipolar magnetic field strength at the pole.

CIAO software (version 4.14; CALDB 4.9.6). We used the latest ACIS gain map, and applied the time-dependent gain and charge transfer inefficiency corrections. The data were then filtered for bad event grades and only good time intervals were used. No high background events were detected, resulting in an exposure time of about 20.1 and 10.1 ks for the first and second observation, respectively.

We did not detect any significant X-ray emission at the radio position of GLEAM-X J1627 when co-adding the two *Chandra* observations (total on-source livetime of 29.8 ks). Specifically, we detected only one photon in the 0.3–8 keV energy range within a  $2''$  error circle centered on the source position. Taking a  $3\sigma$  upper limit of 8.9 photons (Gehrels 1986), we can infer an upper limit on the X-ray quiescent count rate of GLEAM-X J1627 of  $\sim 2.9 \times 10^{-4}$  counts  $s^{-1}$  (at  $3\sigma$  c.l.). We checked this number using different approaches. We extracted source counts from circular regions with a radius of  $0.8''$  (enclosing 90% of the point spread function region at 1 keV),  $2''$  or  $3''$ . For the background, we also assumed different extraction regions: an annulus with an inner radius equal to the source radius and an outer radius 5 times larger, or circles of the same size as the source extraction regions, far from the aim point but located on the same CCD. We used the CIAO SRCFLUX tool to extract the upper

limits of the source count-rate using all the different combinations of source and background extractions. In all cases, the tool gives a  $3\sigma$  limit on the background-subtracted count rate at the position of the radio source of  $3 \times 10^{-4}$  counts  $s^{-1}$  (0.3–8 keV) after merging the event files from the two observations.

## 2.2. Radio observations: MWA, MeerKAT and ATCA

We performed near-contemporaneous radio observations with three different radio telescopes: the MWA, MeerKAT, and ATCA, spanning a frequency range of 170 MHz–9 GHz. We found no pulsed or continuum radio emission at the location of GLEAM-X J1627. The observation properties and the derived ( $3\sigma$ ) upper limits of the flux density are shown in Tab. 1.

### 2.2.1. MWA observations

We observed with the Phase II extended configuration of the MWA using 5-minute pointed snapshots at 170–200 MHz as GLEAM-X J1627 transited (i.e. when the primary beam sensitivity was highest). 104 tiles were functional at the time of observing. We reduced the data using the download, cal-

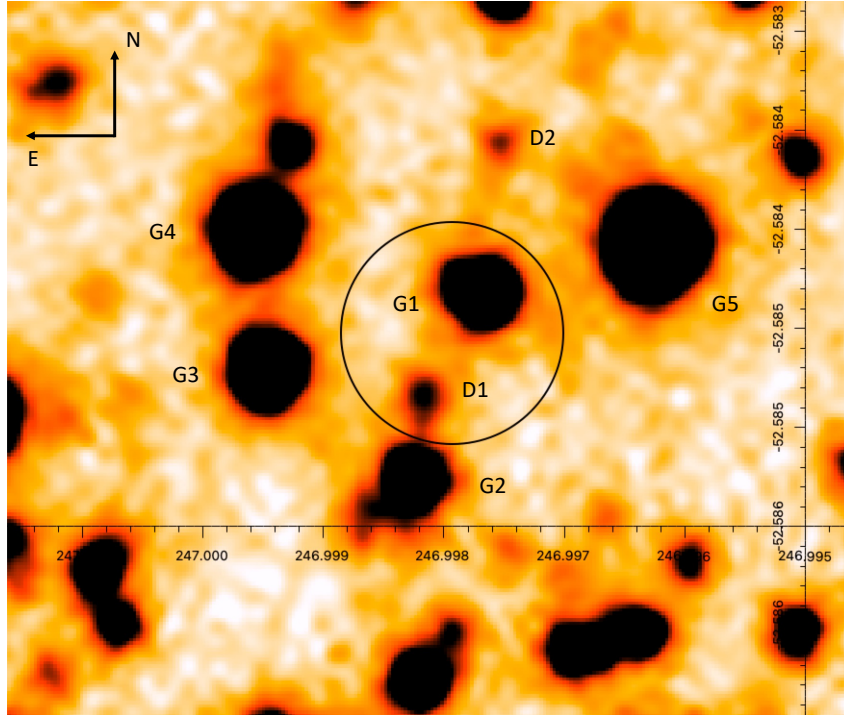


**Figure 2.** The  $z$ -band DECAPS image of the field of GLEAM-X J1627. The position of the radio source and its  $1\text{-}\sigma$  error circle (with a radius of  $2''$ ) are reported. The positions of the five *Gaia* (G1, G2, G3, G4, G5) and two DECAPS (D1, D2) objects within  $4''$  are also reported. North is up and East is left.

ibration, and imaging stages of the GLEAM-X pipeline<sup>1</sup> (Hurley-Walker et al. 2022, in press). Stokes I imaging was performed with WSCLEAN (Offringa et al. 2014) using standard GLEAM-X settings, resulting in a restoring beam size of  $1'$ . Primary beam correction was performed using the most up-to-date MWA beam model (Sokolowski et al. 2017). At these frequencies, the source dispersion measure of  $57 \text{ pc cm}^{-3}$  causes  $\sim 2 \text{ s}$  of smearing across the band, so there is no need to perform dedispersion to make a detection. Since the pulse profile of GLEAM-X J1627 was previously 30–60 s wide, and the integration time is 4 s, we split the data into 32-s intervals and folded at  $P = 1091 \text{ s}$ . No pulsed emission was observed to a  $3\sigma$  limit of  $16 \text{ mJy beam}^{-1}$  per (32 s-long) phase bin. No bright single pulses were observed in any individual timestep, down to a  $3\sigma$  upper limit of  $100 \text{ mJy beam}^{-1}$ . The RMS noise  $\sigma$  in each 5-min snapshot is  $10 \text{ mJy beam}^{-1}$ . By stacking all 222 min of observing time, we obtained a  $3\sigma$  upper limit in the mosaic of  $5 \text{ mJy beam}^{-1}$ .

### 2.2.2. MeerKAT observations

We used MeerKAT in UHF (580 MHz–1.1 GHz) with 8-s time integration. Calibration was provided by the Science Data Processor pipeline at the South African Radio Astronomy Observatory. Dispersion smearing is just 0.5 s, less than

the integration interval. We used WSCLEAN to image the calibrated measurement set, selecting only baselines with lengths  $>573\lambda$ , so as to down-weight contaminating Galactic diffuse emission on scales of  $>0'.1$ . We imaged 9 sq. deg. with a pixel scale of  $1''.8$ , at a ‘‘Briggs’’ robust weighting of 0.0 (Briggs 1995), outputting 10 equally-spaced channels and joining cleaning across them to account for spectral variations across the wide bandwidth due to intrinsic source spectra and the primary beam. We CLEANED down to  $3\times$  the RMS of the residuals, and then down to  $1\times$  the RMS for pixels within regions already selected as containing CLEAN components (`-auto-mask= 3`; `-auto-threshold= 1`). We imaged each 8-s correlator dump with the continuum sources subtracted and detected no single pulses to a  $3\sigma$  limit of  $3 \text{ mJy beam}^{-1}$ . Splitting the data into 32-s intervals and folding at  $P = 1091 \text{ s}$ , no pulsed emission was observed, to a  $3\sigma$  limit of  $300 \mu\text{Jy beam}^{-1}$  per phase bin. The RMS of the time-integrated image is  $28 \mu\text{Jy beam}^{-1}$ . Therefore, we obtained a  $3\sigma$  upper limit on a persistent radio source of  $84 \mu\text{Jy beam}^{-1}$ .

### 2.2.3. ATCA observations

We observed with ATCA simultaneously in the C- (4–6 GHz) and X- (8–10 GHz) bands using the Compact Array Broadband Backend (Wilson et al. 2011). We applied primary (bandpass and absolute flux density scale) calibration solutions derived from PKS 1934-638 and secondary (gain) calibration solutions from PKS 1646-50. Imaging was performed in MIRIAD (Sault et al. 1995). The RMS in the C- and X-band images was 24 and  $20 \mu\text{Jy beam}^{-1}$ , leading to

<sup>1</sup> <https://github.com/tjgalvin/GLEAM-X-pipeline>



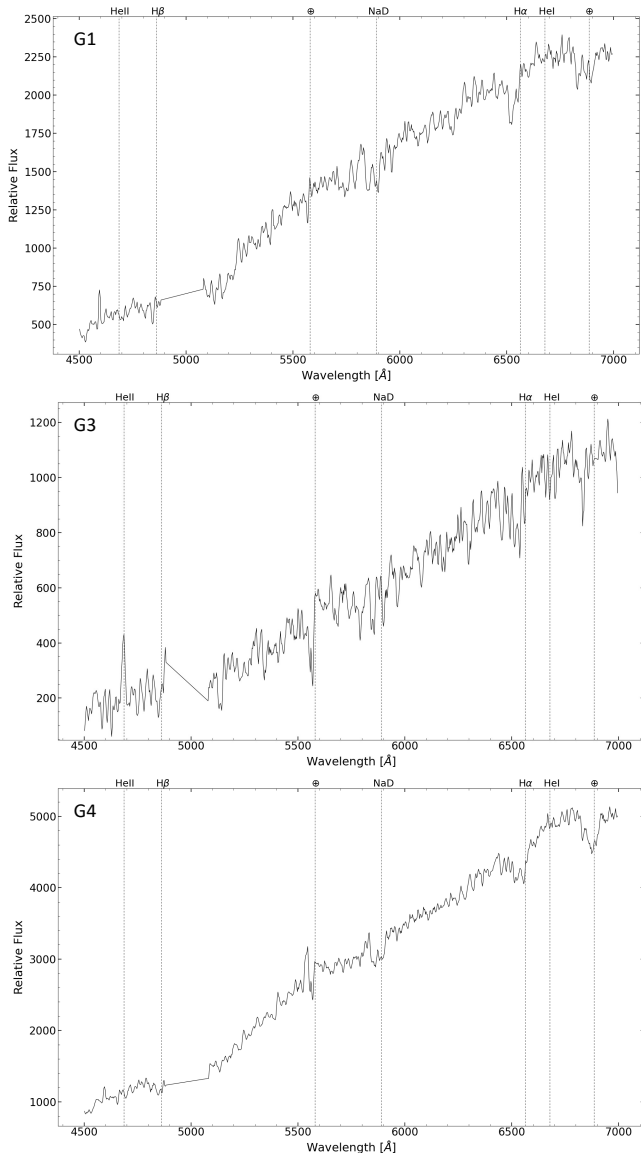


**Figure 3.** From top to bottom: The combined average SALT spectra of G1, G3 and G4 in the range 4500-7000 Å showing absorption features typical of mid-late type stars. The vertical lines report expected hydrogen Balmer ( $H\alpha$  and  $H\beta$ ) and helium lines (HeI and HeII). Telluric features are also marked using an encircled cross. The gap around 5000 Å is due to the mosaicked chips of the RSS detector. A residual artifact is present in the spectrum of G3 around HeII line.

$3\sigma$  upper limits of 72 and 60  $\mu\text{Jy beam}^{-1}$ , respectively. Folding the data resulted in a relatively poor  $3\sigma$  upper limit of 5 mJy  $\text{beam}^{-1}$  due to the imperfect ( $u, v$ )-coverage.

### 2.3. Optical and nIR observations

#### 2.3.1. Archival imaging observations

The field of GLEAM-X J1627 has been observed in the optical band by “The VST Photometric  $H\alpha$  Survey of the Southern Galactic Plane and Bulge” (VPHAS+; Drew et al.

2014). The public VPHAS+ Data Release 4 (DR4) contains several images of the field of GLEAM-X J1627 acquired between 2016 and 2017 with the OmegaCAM imager mounted on the 2.6-m VLT Survey Telescope (VST) in the  $u, g, r$  and  $i$  filters (6, 9, 12 and 6 images, respectively) and narrow band NB\_659 filter centered on  $H\alpha$  (9 images). The single exposures were 150 s for the  $u$  filter, 40 s for the  $g$  filter, 25 s for the  $r$  and  $i$  filters and 120 s for the  $H\alpha$  filter. The calibrated images and derived source catalogues were retrieved from the ESO archive<sup>2</sup>.

The field has also been covered in the optical band by “The DECam Plane Survey” (DECAPS; Schlafly et al. 2018) with the DECAP imager mounted at the Víctor M. Blanco 4-m Telescope in Chile between March 2016 and May 2017 (see Fig. 2). Observations were performed using five broadband filters  $g, r, i, z, Y$ . The single exposures were 96 s for the  $g$  filter and 30 s for the other filters, reaching much deeper limits than VPHAS+ (see Tab. 2). The calibrated images and derived multi-band merged photometry catalogs were retrieved from the DECAPS archive<sup>3</sup>.

The field has been covered in the nIR by “The Vista Variables in the Via Lactea eXtended ESO Public Survey” (VVVX; Minniti et al. 2010). About 200 images were acquired in the  $J, H$  and  $K_s$  filters using the 4-m Visible and Infrared Survey Telescope for Astronomy (VISTA) between July 2016 and September 2019, with single exposures of 10 s for the  $J$  filter, 6 s for the  $H$  filter and 4 s for the  $K_s$  filter adopting different ditherings. The calibrated stacked images and derived catalogs were retrieved from the ESO archive.

We also inspected the *Gaia* early and final Data Releases 3 (eDR3, DR3) (Gaia Collaboration et al. 2021, 2022) to search for a possible optical counterpart within the  $2''$  of the radio position of GLEAM-X J1627 (Hurley-Walker et al. 2022,  $1-\sigma$  confidence) and found one faint ( $m_G=20.24$ ;  $B_p=21.22$   $R_p=19.37$ ) source, here named G1. There are four additional bright *Gaia* objects nearby which we name G2, G3, G4 and G5 (see Tab. 2 for more details). Unfortunately, the parallaxes of these faint *Gaia* stars are undetermined, preventing a comparison with the radio-derived distance of  $1.3 \pm 0.5$  kpc of GLEAM-X J1627 (Babusiaux et al. 2022). The positions of GLEAM-X J1627, the *Gaia* stars and the two other fainter stars detected in the DECAPS survey are displayed on a  $z$ -band DECAPS cutout image in Fig. 2. In Tab. 2 we report the magnitudes of these stars, and to keep uniformity we have used the AB-to-Vega conversion of Fukugita et al. (1996) for the  $g, r, i$  and  $z$  bands and Hewett et al. (2006) for the Y-band.

We searched for optical and nIR sources close to the position of GLEAM-X J1627 in the VPHAS+, DECAPS and VVVX catalogs. None of the *Gaia* stars is detected in the VPHAS+  $u$  band and G2 and G3 are not detected in the VPHAS+  $g$  band. Tab. 2 reports the derived optical ( $g, r, i$  and  $H\alpha$ ) magnitudes of these *Gaia* objects following the prescription for VPHAS+ data releases. Namely, we used the fluxes

<sup>2</sup> <http://archive.eso.org>

<sup>3</sup> <http://decaps.skymaps.info/>

**Table 2.** Magnitudes of the five *Gaia* sources and the two faint optical sources within  $4''$  from the position of GLEAM-X J1627 as derived from the VPHAS+, DECAPS and VVVX public surveys, as well as from recent observations at SALT. Magnitudes are in the Vega system.

Gaia											
Source	R.A. (J2015.5)	Dec. (J2015.5)	$d_{\text{GLEAM}} (")$	$m_G$	$B_p$	$R_p$					
G1	16 <sup>h</sup> 27 <sup>m</sup> 59 <sup>s</sup> .434	-52° 35' 03."58	0.9	20.24	21.22	19.37					
G2	16 <sup>h</sup> 27 <sup>m</sup> 59 <sup>s</sup> .579	-52° 35' 06."96	2.8	20.60	21.72	19.43					
G3	16 <sup>h</sup> 27 <sup>m</sup> 59 <sup>s</sup> .870	-52° 35' 04."98	3.4	20.31	22.02	19.34					
G4	16 <sup>h</sup> 27 <sup>m</sup> 59 <sup>s</sup> .097	-52° 35' 02."71	4.0	18.81	20.04	17.84					
G5	16 <sup>h</sup> 27 <sup>m</sup> 59 <sup>s</sup> .891	-52° 35' 02."44	4.0	19.52	20.57	18.48					
VPHAS+ survey											
Source				$g$	$r$	$i$	$H\alpha$				
G1				21.98(11)	20.30(8)	19.61(8)	20.23(14)				
G2				-	21.11(13)	20.01(11)	20.65(20)				
G3				-	21.08(13)	19.74(9)	20.54(18)				
G4				20.70(5)	18.92(5)	17.97(3)	18.81(5)				
G5				21.49(8)	19.64(6)	18.75(4)	19.55(8)				
DECAPS and VVVX surveys											
Source	R.A. (J2000)	Dec. (J2000)	$d_{\text{GLEAM}} (")$	$g$	$r$	$i$	$z$	$Y$	$J$	$H$	$K_s$
G1	16 <sup>h</sup> 27 <sup>m</sup> 59 <sup>s</sup> .45	-52° 35' 03."5	0.9	21.731(15)	19.906(10)	20.226(11)	19.250(11)	18.256(12)	17.733(28)	17.088(42)	16.784(71)
G2	16 <sup>h</sup> 27 <sup>m</sup> 59 <sup>s</sup> .58	-52° 35' 07."0	2.8	22.432(26)	20.434(15)	19.514(11)	18.942(10)	18.535(17)	17.947(24)	17.542(62)	17.109(90)
G3	16 <sup>h</sup> 27 <sup>m</sup> 59 <sup>s</sup> .87	-52° 35' 05."0	3.4	22.978(45)	20.361(14)	19.047(8)	18.126(7)	17.744(9)	16.870(10)	15.989(14)	15.757(24)
G4	16 <sup>h</sup> 27 <sup>m</sup> 59 <sup>s</sup> .10	-52° 35' 02."7	4.0	20.567(8)	18.649(6)	17.705(6)	17.035(6)	16.750(6)	16.126(7)	15.517(11)	15.311(20)
G5	16 <sup>h</sup> 27 <sup>m</sup> 59 <sup>s</sup> .89	-52° 35' 02."4	4.0	21.221(10)	19.297(8)	18.359(6)	17.677(6)	17.398(8)	16.764(9)	16.185(19)	15.937(28)
D1	16 <sup>h</sup> 27 <sup>m</sup> 59 <sup>s</sup> .56	-52° 35' 05."5	1.4	-	22.664(19)	21.393(41)	20.453(32)	20.056(51)	19.146(63)	18.312(109)	18.152(205)
D2	16 <sup>h</sup> 27 <sup>m</sup> 59 <sup>s</sup> .40	-52° 35' 00."9	3.7	-	22.625(18)	21.671(52)	20.777(42)	20.500(75)	-	-	-
SALT											
Source label				$r'$	$i'$	$z'$					
G1				20.05(3)	19.21(2)	18.64(3)					
G2				21.11(8)	19.54(4)	18.90(5)					
G3				20.32(4)	19.14(2)	18.25(2)					
G4				18.75(1)	17.85(1)	17.21(1)					
G5				19.40(2)	18.48(1)	17.84(2)					
VPHAS+ $5\sigma$ Upper limits											
$u = 21.6 \quad g = 22.8 \quad r = 21.6 \quad i = 20.4 \quad H\alpha = 20.7$											
DECAPS $5\sigma$ and VVVX $3\sigma$ Upper limits											
$g = 23.7 \quad r = 22.9 \quad i = 22.8 \quad z = 22.5 \quad Y = 21.6 \quad J = 19.9 \quad H = 19.0 \quad K_s = 18.2$											

derived with an optimal aperture radius of  $1''$  (Aperture 3), applied aperture, airmass and exposure time correction and adopted the zero points in the Vega system reported in the corresponding image catalogs. On the other hand, all the *Gaia* objects are detected in the DECAPS survey. This survey reaches much fainter magnitude limits (see Tab. 2), allowing us to identify two additional faint sources in the  $r$ ,  $i$ ,  $z$  and  $Y$  filters. These two sources, named D1 and D2, are located at an angular distance of  $1.4''$  and  $3.7''$  from GLEAM-X J1627, respectively (see Fig. 2). Given the large uncertainties in the VPHAS+ photometry, we henceforth use the DECAPS photometry to derive information on the nature of the seven detected sources.

Furthermore, while the same procedure used for VPHAS+ has been adopted to the VISTA image catalogs, the two faint sources, D1 and D2, are not detected in the single images. We then used the nIR PSF photometry recently performed for the VVV survey (Alonso-García et al. 2018) and in particular for the VVVX survey (Alonso-García et al., in preparation) for the sky region of GLEAM-X J1627. The latter is obtained by

stacking all images, making it possible to reach much fainter magnitudes in the  $J$ ,  $H$  and  $K_s$  bands (see Tab. 2).

### 2.3.2. SALT observations

The field of GLEAM-X J1627 has been observed on 2022 April 27 at the 10-m Southern African Large Telescope (SALT; Buckley et al. 2006) equipped with SALTICAM (O'Donoghue et al. 2006) in  $r'$  and  $i'$  SDSS filters, and with the Robert Stobie Spectrograph (RSS; Burgh et al. 2003) in imaging mode with the  $z'$  SDSS filter. Three images for each filter were acquired with exposure times of 120 s ( $r'$  and  $i'$  filters) and 150 s ( $z'$  filter). The  $r'$  and  $i'$ -band acquisitions were performed cyclically ( $r'$ ,  $i'$ ,  $r'$ ,  $i'$ , etc) from 21:37:03 to 21:56:08 UT, while  $z'$ -band exposures were acquired sequentially from 21:24:10 to 21:29:51 UT. A  $2 \times 2$  binning and Faint/Slow mode were adopted for these observations.

Images have been processed with the `Pysalt` pipeline that corrects for bias, cross-talk, gain and amplifier mosaicking. No standard stars were observed and hence no absolute flux calibration was performed due to the moving pupil of the telescope (see Buckley et al. 2008). Therefore, the images were analyzed to obtain differential photometry

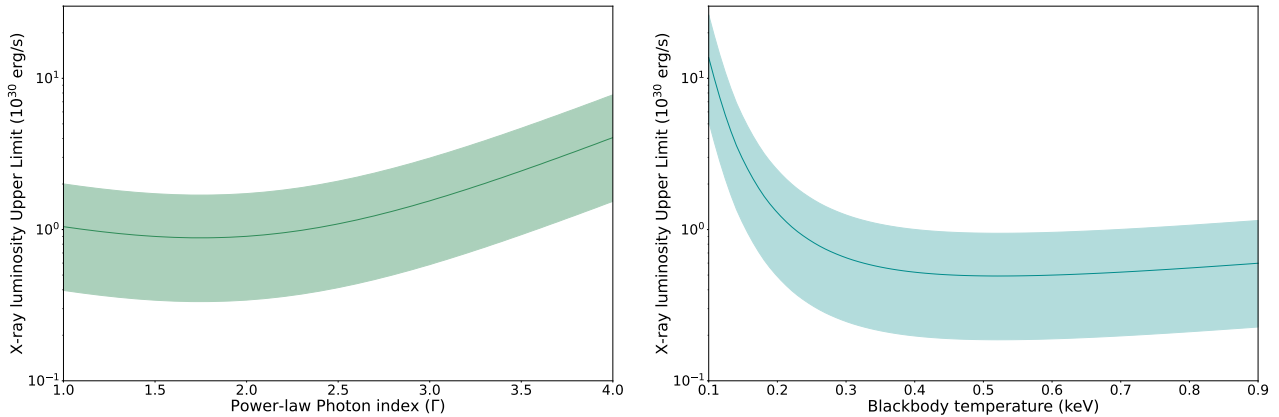


**Figure 4.** Upper limits at  $3\sigma$  confidence level on the X-ray luminosity of GLEAM-X J1627 derived assuming either an absorbed power-law spectrum with  $\Gamma = 1 - 4$  (left panel) or an absorbed blackbody spectrum with  $kT = 0.1 - 0.9$  keV (right panel). The solid curves mark the limits derived assuming a distance of 1.3 kpc, while the shaded areas indicate the range of luminosities that account for the uncertainty in the source distance.

with the bright 2MASS stars 2MASS J16275876–5235170, 2MASS J16280154–5235061 and 2MASS J16275821–5234474 which have stable photometric measurements in DECAPS.

Aperture photometry was performed on each image and on stacked images using the three exposures in each band with the `iraf` task `daophot`. The targets detected in these images are the 5 *Gaia* stars but not the two faint ones found in DECAPS. The differential instrumental magnitudes were then converted into  $r$ ,  $i$  and  $z$ -filter magnitudes using the DECAPS magnitudes of the bright stars. Since the *Gaia* stars do not show variability within their photometric uncertainties, in Tab. 2 we report their magnitudes obtained from the stacked images. The associated uncertainties are statistical only. The results of the photometry of the *Gaia* stars appear consistent with the magnitudes obtained from DECAPS. The lack of detection of the two faint DECAPS sources is due to a shallower limiting magnitude.

Two low-resolution spectra, with a 30-minute exposure each, were acquired with the RSS mounted on *SALT* in long-slit mode. The first spectrum was taken starting on 2022 Feb 11 at 02:35:49 UT, while the second one starting on 2022 Feb 12 at 02:12:42 UT. The PG0300 (300 l/mm) grating was used with a tilt angle of  $5.75^\circ$ , yielding an usable wavelength range of  $\sim 3900\text{--}9000$  Å and a resolving power of  $R \simeq 600$  at 5000 Å. We used the  $1''.5 \times 8'$  long-slit placed at a position angle of  $\text{PA} = 290^\circ$  (measured from north to east) for both observations to pass through stars G1, G3, and G4 (see Fig. 3). The spectra were reduced using standard `iraf` tasks including flat-field, background subtraction and cosmic-ray removal. The wavelength calibration was performed using an Ar arc lamp. No standard stars were observed and thus the spectra were not calibrated in flux.

### 3. RESULTS

#### 3.1. X-ray and radio

Using the HEASARC PIMMS tool, we estimated the  $3\sigma$  upper limit on the source X-ray flux assuming different spectral models. The expected absorption column density  $N_{\text{H}}$  from the  $N_{\text{H}}\text{--DM}$  relation by He et al. (2013) is  $N_{\text{H}} \simeq 2 \times 10^{21} \text{ cm}^{-2}$  using a  $\text{DM} = 57 \text{ pc cm}^{-3}$ . We derived an upper limit on the 0.3–10 keV absorbed (unabsorbed) flux of  $3.1(4.5) \times 10^{-15} \text{ erg cm}^{-2} \text{ s}^{-1}$  and  $2.0(3.2) \times 10^{-15} \text{ erg cm}^{-2} \text{ s}^{-1}$  ( $3\sigma$  c.l.) for a power-law with  $\Gamma = 2$  and a blackbody with  $kT = 0.3$  keV, respectively. Assuming that the source is at a distance of 1.3 kpc (as derived from its DM), these values translate into a luminosity limit of  $9.1 \times 10^{29} \text{ erg s}^{-1}$  for a power-law spectrum and  $6.5 \times 10^{29} \text{ erg s}^{-1}$  for a blackbody spectrum. To take into account the uncertainties related to the assumed spectral model, we make the same estimates as above but assume an absorbed power-law spectrum with a photon index ranging from  $\Gamma = 1 - 4$ , as expected for rotation-powered pulsars, and an absorbed thermal spectrum modelled by a blackbody with temperature between  $kT = 0.1 - 0.9$  keV, typical of a magnetar in quiescence (Rea & Esposito 2011; Coti Zelati et al. 2018). In Fig. 4 we plot our upper limits as a function of the different assumed spectral shapes, accounting also for the uncertainty on the distance ( $1.3 \pm 0.5$  kpc).

The  $3\sigma$  upper limits on the radio flux density at our observed frequencies are given in the final column of Tab. 1, with a strong limit of  $\lesssim 100 \mu\text{Jy beam}^{-1}$  at GHz frequencies.

#### 3.2. Optical and nIR

Fig. 3 shows the optical spectra of G1, G3 and G4. These spectra do not reveal emission lines that could point to an interacting binary or to the presence of deep absorption features from a hot companion star, such as a white dwarf. Note that a sky artifact is present at HeII for the G3 star. The *SALT* spectra were compared with the stellar spectral library of Jacoby et al. (1984), which first suggest a spectral type around mid/late G for G1, a late-G or early-K star for G3 and a late F

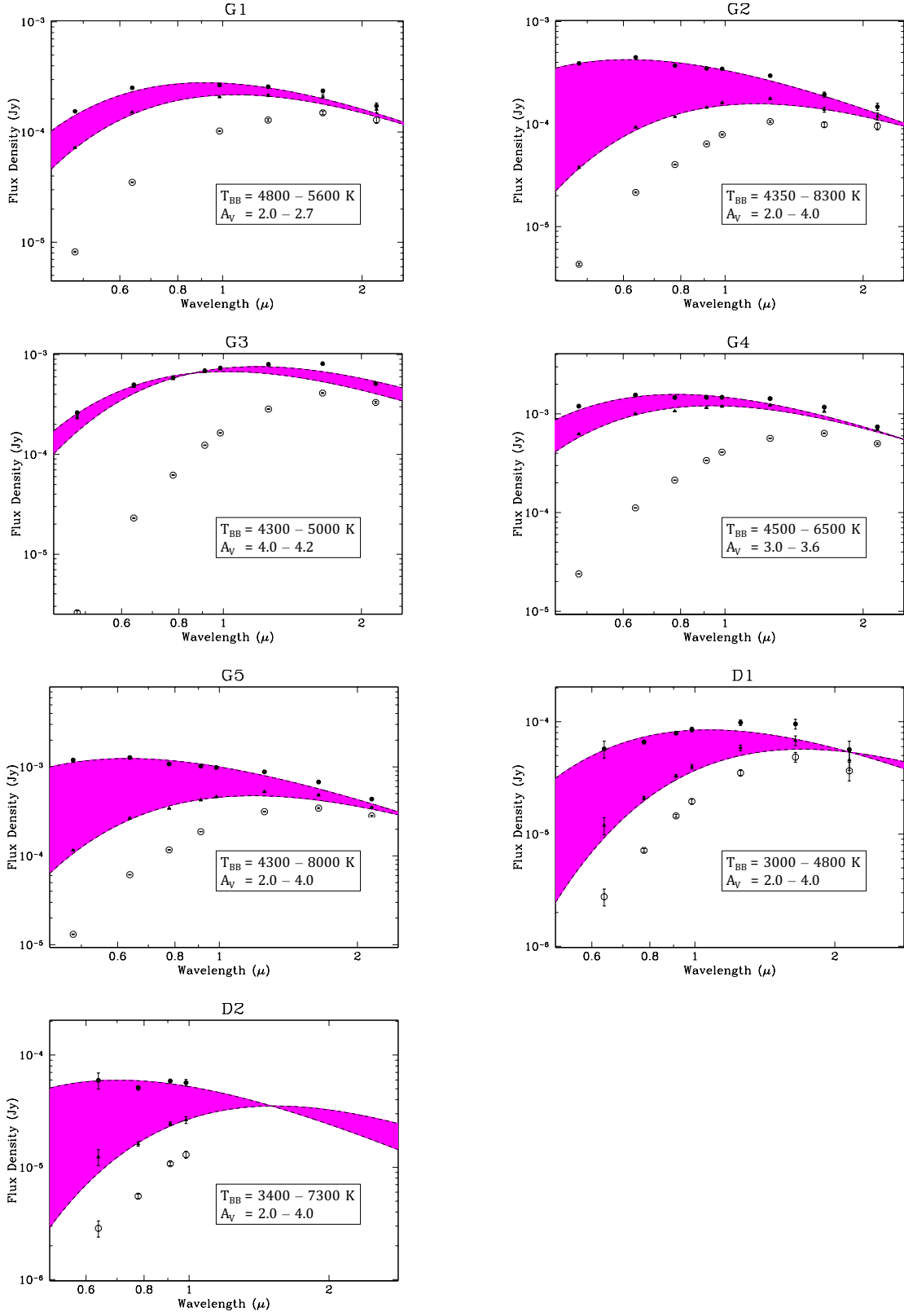


**Figure 5.** From left to right, top to bottom: SEDs of G1, G2, G3, G4, G5, D1 and D2 adopting different extinction corrections, shown with their best-fitting blackbody models. The open circles report the SEDs without reddening corrections, while the filled triangles and circles report the SEDs corrected for the low and high values of extinctions  $A_V$ , respectively, as reported in the text (see also § 3.2). The shaded magenta areas comprise the range of blackbody temperatures and extinctions.



or early/mid G for G4. The low resolution of the spectra does not allow us to better constrain the nature of these stars. In aid of these, we have compared the observed VPHAS+ and DECAPS ( $g-r, r-i$ ) colors with the VST/OmegaCAM synthetic colors for main sequence stars tabulated in [Drew et al. 2014](#) for extinctions  $A_V$  from 0 to 8 in steps of 2 and adopting the mean Galactic reddening law  $R_V = 3.1$ . The total extinction in the direction of the source is estimated to be  $A_V = 4.15$  ([Schlafly & Finkbeiner 2011](#)). However, the observed colors do not match a single sequence, indicating that these stars suffer different extinctions likely due to different distances. The same is true for the nIR ( $J-H, H-K$ ) colors when compared to the main sequence stars in the 2MASS  $J$ ,  $H$  and  $K_s$  bands by [Straižys & Lazauskaitė \(2009\)](#) applying extinctions ranging from  $A_V = 0, 2$  and  $4$  and using the VISTA calibration from 2MASS ([González-Fernández et al. 2018](#)). Given the deeper and more accurate DECAPS photometry and the PSF VISTA nIR photometric measurements, we extracted the spectral energy distributions (SEDs) for each of the seven stars applying an extinction correction from  $A_V$  2 to 4.

Fig. 5 reports the SEDs for these objects together with the best fitting blackbody functions for each extinction correction. The SEDs are constructed with few measurements, giving a low quality of the fits ( $\chi_{\text{red}}^2$  ranging from 5 to 10). Given the unknown distance and thus reddening, and relying on the optical spectra acquired for G1, G3 and G4, we tentatively ascribe for G1  $A_V$  between 2 and 2.7 with temperature in the range 4800–5600 K and thus a mid G to early K spectral type; for G3  $A_V \sim 4$  with temperature  $\sim 4300$  K and thus a mid K spectral type, slightly later than estimated from spectra, or otherwise a higher reddening  $A_V \sim 4.2$  to match a late G or early K type; for G4  $A_V$  should be between  $\sim 3$ – $3.8$  with temperature  $\sim 5500$ – $6300$  K to match the late F or mid G spectral type. For G2 we do not have spectra to constrain the spectral type and thus the extinction,  $A_V$ , could be between 2–4. This gives a wide range of temperatures,  $\sim 4400$ – $8300$  K, which correspond to spectral types ranging from mid or late A to mid K. The case of G5 is similar. Therefore, for  $A_V$  between 2–4, the temperature would result in the range 4300–8000 K spanning spectral types between late A to mid K. Also, for D1 and D2, an extinction  $A_V$  between 2 and 4 would result in blackbody temperatures in the range 3000–4800 K and 3400–7300 K, respectively. The spectral types of these two faint objects, if they are main sequence stars, would range from mid M to early K and from mid M to early F, respectively.

#### 4. DISCUSSION

In this work, we have presented simultaneous X-ray and radio observations of the 18-min radio transient GLEAM-X J1627, and deep optical and nIR observations of the field.

We have derived the deepest X-ray upper limits on its emission, an important ingredient in constraining its nature. The exact X-ray luminosity limit strongly depends on the assumed spectral shape and distance: we hereafter assume

$L_X \leq 10^{30} \text{ erg s}^{-1}$  as an average value over the different spectral models and distance errors (see Fig. 4 for the exact calculations). The radio limit in quiescence we have derived from the MeerKAT observations, assuming isotropic emission and a flat spectrum in the observing radio band, resulted in a quiescent radio luminosity limit of  $L_{\text{radio}} \leq 10^{25} \text{ erg s}^{-1}$ . This radio limit is very low but not unusual in the pulsar population (see also Fig. 6). We note that these limits are derived under strong assumptions, which may not necessarily be correct, but are only presented to give an idea of the order of magnitude.

Furthermore, the optical and nIR observations of the field revealed several objects potentially compatible with the source position (see Fig. 2), that we discuss in the following sub-sections.

##### 4.1. The transient periodic radio emission in the framework of radio magnetars

The observed radio characteristics of GLEAM-X J1627, namely its transient radio emission, its bright and variable single peaks, the pulse profile variability, and its high linear radio polarization ([Hurley-Walker et al. 2022](#)), are perfectly in line with what is typically observed for radio-loud magnetars. In fact, radio emission in magnetars is typically observed in coincidence with their X-ray outbursts, and with large variability in terms of luminosity and shape of their single peaks (see [Esposito et al. 2021](#) for a recent review, and references therein). The non-detection of an X-ray outburst at the time of GLEAM-X J1627’s radio activation is not surprising, since it might have been easily missed due to the sparse and shallow coverage of the large-field-of-view X-ray monitors. The only apparent inconsistency between GLEAM-X J1627 and the population of radio-loud magnetars is thus far its 18-min periodicity (see Fig. 1).

However, as extensively studied by [Ronchi et al. \(2022\)](#), the 18-min periodicity of GLEAM-X J1627’s radio emission cannot be reconciled with the pulsar scenario when only dipolar losses and a typical crust+core field configuration are considered. This would require the assumption that this pulsar has an unreasonably large magnetic field ( $B \sim 10^{16} - 10^{17} \text{ G}$ ) that does not decay in time (something unseen in the pulsar population; see also Fig. 1 by [Ronchi et al. 2022](#)). In a typical crust+core field configuration, the magnetic field is expected to decay on a time scale of 10–100 kyr depending on its intensity (the stronger the field, the faster it decays; see the spin-period evolutionary curves in Fig. 1).

A more plausible possibility is that fall-back accretion from the supernova could easily have slowed a magnetar with a magnetic field of  $\sim 10^{13}$ – $10^{14} \text{ G}$  down to its current period of 18 min in  $\sim 10^4$ – $10^6 \text{ yr}$ . In this scenario, the supernova fossil-disk is now inactive (because the disk is now too cold or has been completely disrupted), so the source had resumed its dipolar-driven rotation and normal radio-loud magnetar activity. However, its spin period has been driven at a longer value than that of its peers at the same age and field

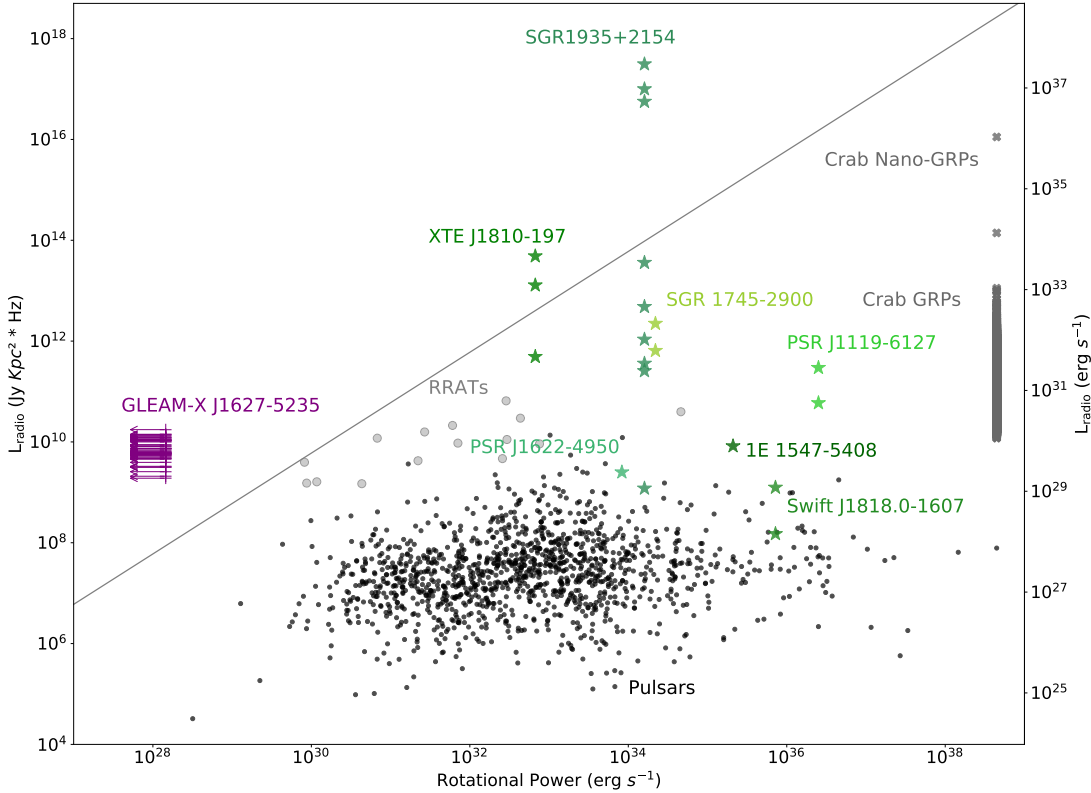


**Figure 6.** Radio luminosity versus rotational power of bright single peak emission for all pulsar classes and the GLEAM-X J1627’s upper limits. Radio magnetars’ bright single pulses are labelled in green. The gray solid line marks the relation  $L_{\text{radio}} = \dot{E}_{\text{rot}}$ .

( $\sim 10^{14} - 10^{15}$  G; for detailed simulations, see Ronchi et al. 2022 and Gençali et al. 2022; Tong 2022).

Several studies discussed the radio luminosity of GLEAM-X J1627 during its radio outburst in comparison with the limits of its rotational energy (Hurley-Walker et al. 2022; Erkut 2022). In particular, assuming isotropic emission, the radio luminosity of the brightest single peaks ( $L_{\text{radio}} \sim 10^{30} - 10^{31}$  erg s $^{-1}$ ; Hurley-Walker et al. 2022) exceeds the limits on the rotational power of the source by a few orders of magnitude. Fig. 6 shows those peak radio luminosities and the rotational power of GLEAM-X J1627 in comparison with other pulsars, rotating radio transients (RRATs) and radio-loud magnetars. For the radio-loud magnetars, given their large variability, we have chosen the brightest radio pulses reported in the literature (data collected from Camilo et al. 2006, 2007; Weltevrede et al. 2011; Deller et al. 2012; Lynch et al. 2015; Majid et al. 2017; Pearlman et al. 2018; Lower et al. 2020; Esposito et al. 2021). It is well known that assuming isotropic radio emission is not realistic, and a beaming factor necessarily has to be present (see e.g. Erkut 2022). However, the relation between the duty cycle and the spin period of canonical pulsars has a large spread (Manchester et al. 2005). Moreover, it is observed that this relationship does not apply to radio-loud magnetars, which in

general show larger duty cycles than what one would expect from the extrapolation of this tentative relation for radio pulsars to magnetars (see i.e. Camilo et al. 2006, 2007). To avoid the uncertainty of beaming models, which for magnetars are mostly unknown even theoretically, we plotted the isotropic radio luminosity for all the different pulsar classes in Fig. 6. From this plot, at variance with canonical radio pulsars, we see how the brightest single peaks for radio-loud magnetars might exceed their rotational powers, in line with what is possibly observed for GLEAM-X J1627. While not resolving uncertainties related to the exact mechanism of radio emission or the beaming factor, Fig. 6 shows that, under the assumption of isotropic emission, even for magnetars the brightest single peaks exceed their rotational energy budget. Considering all the uncertainties in the assumptions used to derive the radio luminosities plotted in Fig. 6, GLEAM-X J1627’s radio luminosity excess over its rotational power cannot be used as an argument for or against its neutron star nature.

Furthermore, in Fig. 7 we report the radio-transient plane (Cordes et al. 2004; Pietka et al. 2015) where we include the brightest radio single peaks observed in radio-loud magnetars and compare them with GLEAM-X J1627 and other classes of radio-emitting sources (data collected from Pietka et al.

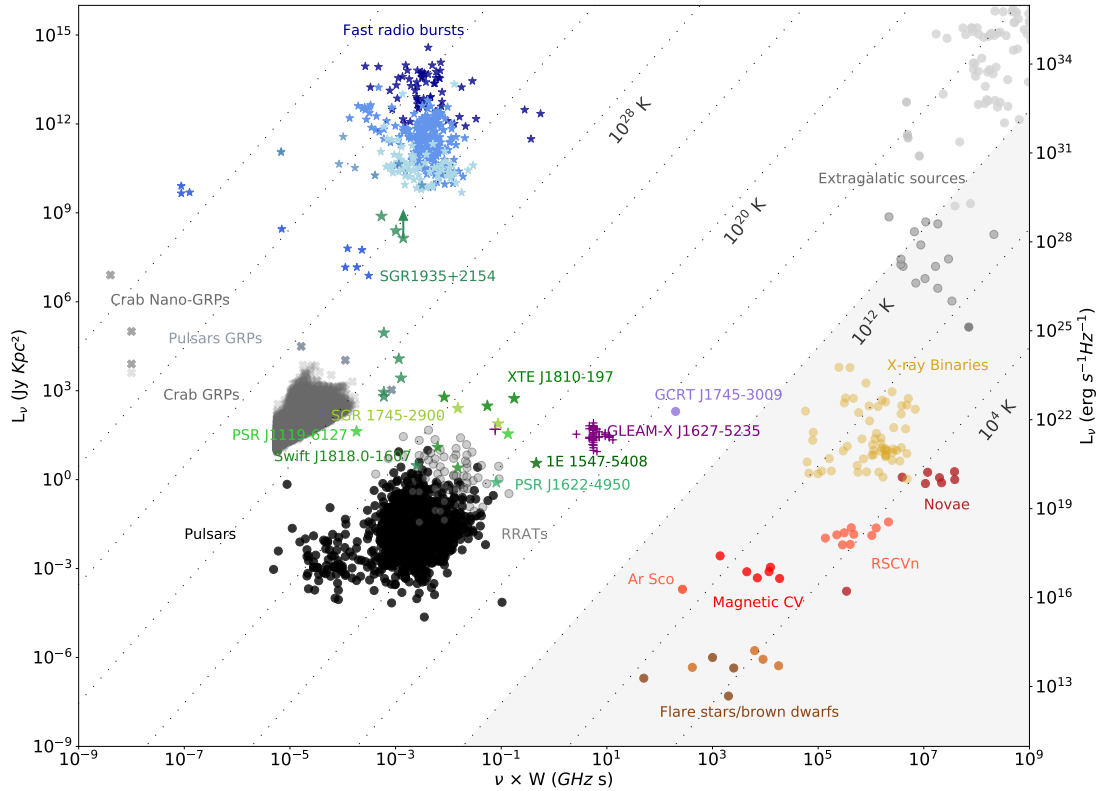


**Figure 7.** Radio-transient plane including all transient sources with a particular focus on radio magnetars’ bright single pulses (different green tones), GLEAM-XJ1627 (violet) and white dwarf systems (different red tones). Data collected from: Camilo et al. (2006, 2007); Weltevrede et al. (2011); Deller et al. (2012); Lynch et al. (2015); Majid et al. (2017); Pearlman et al. (2018); Lower et al. (2020); Esposito et al. (2021); Pietka et al. (2015); Marsh et al. (2016); Keane (2018); Nimmo et al. (2022).

2015; Marsh et al. 2016; Keane 2018; Nimmo et al. 2022). On the x-axis we report the product of the transient emission duration (or pulse width) times the frequency at which it was observed, and on the y-axis the observed flux density times distance squared. The shaded grey area, starting from brightness temperatures of  $T_b < 10^{12}$  K, divides the coherent and incoherent emission processes in the Rayleigh-Jeans approximation (Cordes et al. 2004; Pietka et al. 2015). As reported by Hurley-Walker et al. (2022), the radio emission of GLEAM-X J1627 occupies a region on the plane compatible with being powered by a coherent process, as also observed in other radio pulsars and radio-loud magnetars.

#### 4.2. Neutron star cooling models compared with the X-ray upper limits

The X-ray upper limits that we derived for GLEAM-XJ1627 might be used to constrain its age and field configuration in the pulsar scenario. In particular, the magnetic field of a pulsar is expected to heat the neutron star crust via the dissipation of currents, which depends on the crustal microphysics, the pulsar magnetic field strength and configuration, and the star’s age. To compare our X-ray

upper limits with neutron star cooling curves, we used a 2D magneto-thermal evolution code (Aguilera et al. 2008; Pons et al. 2009; Viganò et al. 2012; Viganò et al. 2013, 2021).

This 2D code assumes a background structure for the star in order to calculate necessary microphysical ingredients, such as the electron density  $n_e$ , thus providing realistic magneto-thermal information. A comprehensive revision of the microphysics embedded in magneto-thermal models is given by Potekhin et al. (2015). In this study, we have used the 2D magneto-thermal code to run a set of cooling models using different initial configurations. We considered: (i) crust-confined fields: the radial component of the magnetic field vanishes at the crust-core interface, while the latitudinal ( $B_\theta$ ) and toroidal ( $B_\phi$ ) components are different from zero; (ii) core-dominated fields: the radial component of the magnetic field is  $B_r \neq 0$  at the crust-core interface, and the magnetic field lines penetrate the core. In both cases, at the stellar surface, the magnetic field is matched continuously with the potential solution of a force-free field (i.e. the electric currents do not leak into the magnetosphere). The cooling

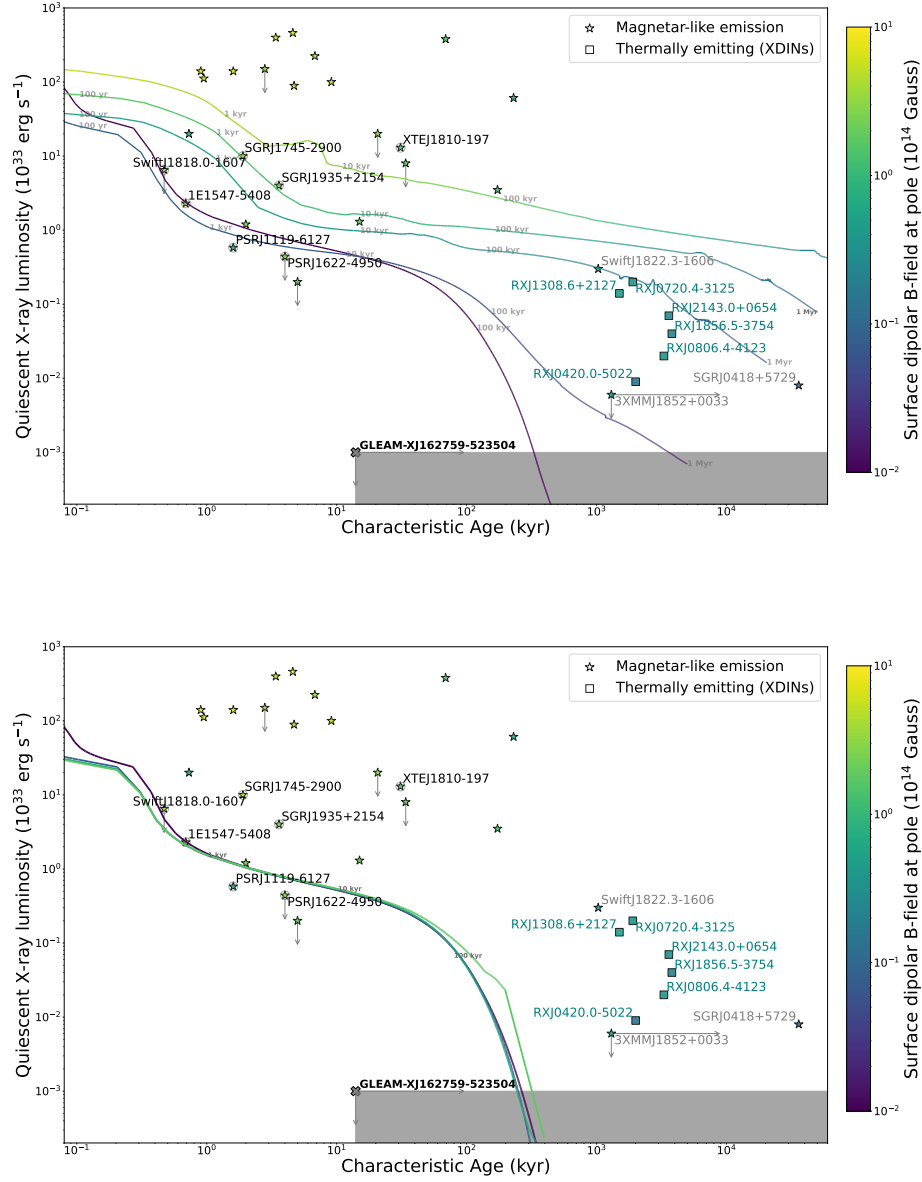


**Figure 8.** Evolutionary tracks for crust-dominated (top panel) and core-dominated (bottom panel)  $B$ -field configurations superimposed on the X-ray luminosity of different pulsar classes, in particular radio-loud magnetars (labelled using a gray circle), XDINSs (in light blue) and low-field magnetars (labelled using gray names). The shaded region corresponds to the limits on the X-ray luminosity and the characteristic age derived for GLEAM-X J1627.

models use the Sly4<sup>4</sup> equation of state (Douchin & Haensel 2001) with a mass of  $1.4 M_{\odot}$  and the envelope model of Gudmundsson et al. (1983). The initial magnetic field ranges from  $10^{12}$  G up to  $10^{15}$  G for the dipolar poloidal component at the pole of the star, whereas the toroidal component accounts for about 40–50% of the total magnetic energy in the system. Note that we have neglected neutrino-synchrotron

cooling in these simulations, as this effect requires further examination which is planned in the future.

Fig. 8 shows the comparison of the 2D magneto-thermal models for crustal (top panel) and core-confined (bottom panel) field configurations, superimposed on the X-ray emission of different pulsar classes, in particular radio magnetars, normal X-ray emitting pulsars, X-ray Dim Isolated Neutron Stars (XDINSs) and low-field magnetars (data updated from Viganò et al. 2013 to be published in Dehman et al. in prep.). In the typical scenario of a crust-confined field configuration,

<sup>4</sup> <https://compose.obspm.fr/>

the X-ray limits we derive for GLEAM-X J1627 are hardly compatible with any radio magnetar known so far. Even the oldest representatives of the magnetar class, the low-field magnetars, have a quiescent emission at ages  $< 10^6$  yr that is brighter than our limits for GLEAM-X J1627. On the other hand, we must remark that significant (observable) Joule heating effects in magnetars are only evident for crustal confined models: if the currents are mostly located in the neutron star core, Joule heating is very ineffective (most energy is lost through neutrino emission). Hence, any of the fast cooling mechanisms discussed in the literature may be reconciled with magnetar-like fields with very low luminosities in the core-field scenario (see Anzuini et al. 2022 for a similar discussion).

#### 4.3. Optical/nIR constraints and the possible white dwarf nature of GLEAM-X J1627

The optical and nIR observations we report here might provide information on the possibility that GLEAM-X J1627 is a binary system harbouring a slowly spinning magnetic white dwarf, given the detected radio periodicity. Radio periodic emission has so far only been observed from the white dwarf pulsar binary AR Sco (Marsh et al. 2016), although AR Sco is not known to display powerful transient radio pulses and this emission is clearly not coherent (unlike GLEAM-X J1627; see also Fig. 7).

Within the  $2''$  positional uncertainty, there are two optical sources, G1 and D1. Within  $4''$  there are five other objects. The *Gaia* parallaxes for the brighter five stars are undetermined, precluding a comparison with the radio distance of GLEAM-X J1627. Adopting an extinction  $A_V$  in the range between 1.0 and 4.1 and a distance estimate of  $1.3 \pm 0.5$  kpc, the positions of the *Gaia* stars in the *Gaia* HR diagram do not match the white dwarf sequence, but fall on the main sequence of mid-late type stars for  $A_V = 1$  and 2, or below it for  $A_V = 4$  (see also the left panel of Fig. 9). Indeed, the optical spectra acquired at *SALT* for G1, G3 and G4, the optical colors and the absence of detection in the  $u'$  band, suggest that these optical sources are mid-late-type stars (see the left panel of Fig. 9, where the positions of the five *Gaia* objects are shown in black for  $A_V = 4.1$  and in magenta for  $A_V = 1$ ). Assuming their tentative spectral types and taking into account the uncertainty in the extinction, we can place lower limits on the distances of these *Gaia* stars adopting the corresponding  $V$ -band absolute magnitudes and the *Gaia* DR3 conversion formulas<sup>5</sup>: for G1  $d > 3.7$  kpc, for G2  $d > 3.9$  kpc, for G3  $d \geq 1.6$  kpc, for G4 and G5  $d > 2.2$  kpc. We also note that the distances obtained for these *Gaia* sources by Bailer-Jones et al. (2021) using a Galactic prior model give lower limits of 3-4 kpc. We therefore conclude that these stars are unlikely to be emitting white dwarfs, and that only source G3 and possibly sources G4 and G5 might have distances compatible with GLEAM-X J1627. Similar conclusions were

drawn using the *Gaia* proper motions and constructing a reduced proper motion diagram given the large uncertainties in extinctions, expected absolute magnitudes and proper motions. However, this does not rule out the possibility of these sources being mid-late type companion stars of a binary white dwarf system similar to AR Sco. Given our nIR limits, we can only rule out such a system for  $A_V \leq 2$ .

The distances of the faint objects D1 and D2 cannot be constrained either. Their SEDs indicate that they are cool objects with temperatures between 3000 and 7300 K (see Fig. 5). If they were main sequence stars, their distances would be  $> 3.3$  kpc for D1 and  $> 4.4$  kpc for D2. Therefore, we can reliably exclude that they are companion stars of a white dwarf binary system. Similarly, the hypothesis that GLEAM-X J1627 could be a hot and bright magnetic subdwarf star located at 1.3 kpc (Loeb & Maoz 2022) would be difficult to reconcile with the lack of detection in the DECAPS survey. We also note that the hot subdwarf stars (sdO/B type) identified by *Gaia* within 1.5 kpc have absolute magnitudes between -1 and 7 in the  $G$ -band (Geier et al. 2019) and are typically not highly magnetic. At the estimated distance of GLEAM-X J1627, such a star would have been detected.

The possibility that GLEAM-X J1627 may be an isolated magnetic white dwarf pulsar located at 1.3 kpc is less constrained. Such a star would only be detected in the optical/nIR observations if it is hot (with a temperature  $> 10000$  K) and has a low extinction of  $A_V \sim 2$ . The right panel of Fig. 9 shows the masses and temperatures of detected isolated magnetic white dwarfs with our DECAPS limit ( $r > 22.9$ ) superimposed as a dotted line (Vennes et al. 2011; Kawka & Vennes 2012; Ferrario et al. 2020). Therefore, we cannot rule out a scenario of an isolated, cooler white dwarf.

## 5. CONCLUSIONS

In the magnetar scenario, the upper limits we have derived on the X-ray luminosity ( $L_X < 10^{30}$  erg s<sup>-1</sup>) imply that GLEAM-X J1627's age should be  $> 1$  Myr for any reasonable crustal magnetic field ( $B > 10^{13}$  G). The 18-min spin period (assuming a fast rotating pulsar at birth) would necessarily require a strong magnetic field and a phase of fossil-disk accretion (see Ronchi et al. 2022), but in any case the age of GLEAM-X J1627 is constrained to be two orders of magnitude higher than that of typical radio-loud magnetars (which have ages  $< 20$  kyr). At this age, the bright radio bursts emitted by GLEAM-X J1627 would be unusual for such an old magnetar. However, it is important to note that the radio emission of GLEAM-X J1627 is instead in line with what has been observed for the known population of radio-loud magnetars (which are younger). The excess of its radio luminosity over the rotational power limits is not unprecedented in the bright single pulses from radio magnetars, despite the unavoidable uncertainty due to the radio beaming factor (see Fig. 6). We also note that, if the magnetar has a core-dominated magnetic field or has witnessed unusual fast cooling (both effects have never been unambiguously ob-

<sup>5</sup> See Tab. 5.8 of the *Gaia* DR3 data guide (<https://gea.esac.esa.int/archive/documentation/GDR3/>).



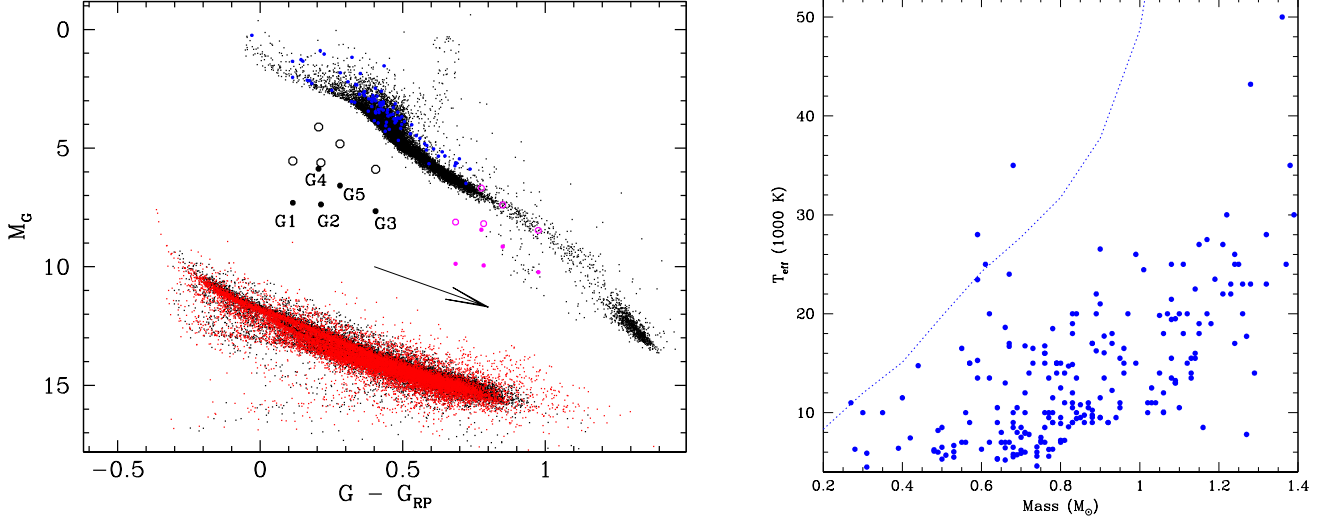


**Figure 9.** *Left panel:* Color-magnitude diagram of the five *Gaia* stars adopting a distance range between 0.8 kpc (filled circles) and 1.8 kpc (empty circles) and extinctions  $A_V = 1.0$  (magenta) and  $A_V = 4.1$  (black). The small dots represent the stars in the color-magnitude diagram retrieved from the *Gaia* DR3 archive within 100 pc and negligible extinction ( $A_G < 0.04$ ). Those flagged as non-single stars are shown in blue. The white dwarfs within 100 pc from the *Gaia* DR2 catalogue of Torres et al. (2019) are reported as black dots and the white dwarfs within 100 pc from the *Gaia* eDR3 catalogue with a probability  $> 90\%$  of being a white dwarf (Gentile Fusillo et al. 2021) are reported as red dots. An extinction vector  $A_V = 2$  is also reported. *Right panel:* Mass and temperature for known magnetic isolated white dwarfs from Ferrario et al. (2020) compared to the upper limit of  $r > 22.9$  at  $5\sigma$  obtained by DECam (blue dotted line).

served in a pulsar or a magnetar), the observed X-ray upper limits would be compatible with a younger age (see Fig. 8). The field in the core is expected to decay on timescales of 1–10 Myr, hence the source’s spin period would initially evolve with a seemingly constant magnetic field (see Fig. 1). In this case, to explain the 18-min spin period, we would need a constant field of  $B \sim 10^{15}$  G for  $\sim 10^8$  yr (or  $B \sim 10^{16}$  G for  $\sim 10^6$  yr), which is rather extreme when compared to the known magnetar population in our Galaxy. In contrast, assuming fall-back accretion, the spin period can easily be reconciled with a 18-min value (Ronchi et al. 2022). Although the core-dominated field-decay interpretation or a fast cooling scenario are in principle viable, they are intriguing, as we have no evidence of other pulsars that require either hypothesis to explain their emission and spin period.

In the magnetic white dwarf scenario, our nIR and optical studies put some constraints on the binary or isolated white dwarf interpretation of GLEAM-X J1627. In particular, none of the sources detected within its positional uncertainty could be unambiguously catalogued as a white dwarf or the companion star of a binary white dwarf system at 1.3 kpc. An AR Sco-like system could pass unnoticed if it has a relatively large extinction. Furthermore, we exclude the possibility of GLEAM-X J1627 being a hot, bright magnetic sub-dwarf star, but cannot rule out an isolated, cooler white dwarf. We note that the rotation periods of magnetic white dwarfs are typically longer than 1 h, with a few spinning at faster rates (Kilic et al. 2021; Schwab 2021), which are believed to be the results of the merger of a double white dwarf system. Therefore a cool isolated white dwarf would need to be sufficiently

magnetic, hence probably with a large mass and small radius, to produce the coherent and pulsed radio emission observed by GLEAM-X J1627.

We gratefully acknowledge the help of D. Minniti and J. Alonso-García in providing the VVVX nIR catalogue in advance. We thank A. Possenti for starting the literature search for some of the bright radio magnetar single pulses presented in this work, and the anonymous referee for her/his careful reading and useful comments that improved our manuscript. NR, FCZ, CD, MR, VG, CP, AB and EP are supported by the ERC Consolidator Grant “MAGNESIA” under grant agreement No. 817661, and National Spanish grant PGC2018-095512-BI00. FCZ, AB and VG are also supported by Juan de la Cierva Fellowships. CD, MR and CA’s work has been carried out within the framework of the doctoral program in Physics of the Universitat Autònoma de Barcelona. NHW is supported by an Australian Research Council Future Fellowship (project number FT190100231) funded by the Australian Government. DdM acknowledges financial support from the Italian Space Agency (ASI) and National Institute for Astrophysics (INAF) under agreements ASI-INAF I/037/12/0 and ASI-INAF n.2017-14-H.0 and from INAF “Sostegno alla ricerca scientifica main streams dell’INAF”, Presidential Decree 43/2018 and from INAF “SKA/CTA projects”, Presidential Decree 70/2016. DB acknowledges support from the South African National Research Foundation. DV is supported by the ERC Starting Grant “IMAGINE” under grant agreement No. 948582. This work was also partially supported by the program Unidad de Excelen-

cia Maria de Maetzu de Maeztu CEX2020-001058-M and by the PHAROS COST Action (No. CA16214).

This research has made use of the services of the ESO Science Archive Facility. This work has made use of data from the European Space Agency (ESA) mission *Gaia* (<https://www.cosmos.esa.int/gaia>), processed by the *Gaia* Data Processing and Analysis Consortium (DPAC, <https://www.cosmos.esa.int/web/gaia/dpac/consortium>). Funding for the DPAC has been provided by national institutions, in particular the institutions participating in the *Gaia* Multilateral Agreement. This work is based on: data products from observations made with ESO Telescopes at the La Silla Paranal Observatory under programme ID 177.D-3023, as part of the VST Photometric H $\alpha$  Survey of the Southern Galactic Plane and Bulge (VPHAS+, [www.vphas.eu](http://www.vphas.eu)); data products from VVVX Survey observations made with the VISTA telescope at the ESO Paranal Observatory under programme ID 198.B-2004. The SALT observations were obtained under the SALT Large Science Programme on transients (2018-2-LSP-001; PI: DB) which is also supported by Poland under grant no. MNiSW DIR/WK/2016/07. The MeerKAT telescope is operated by the South African Radio Astronomy Observatory, which is a facility of the National Research Foundation, an agency of the Department of Science and Innovation. The Australia Telescope Compact Array is part of the Australia Telescope National Facility (<https://www.atnf.csiro.au/>) which is funded by the Aus-

tralian Government for operation as a National Facility managed by CSIRO. We acknowledge the Gomeri people as the traditional owners of the Observatory site. This scientific work makes use of the Murchison Radio-astronomy Observatory, operated by CSIRO. We acknowledge the Wajarri Yamatji people as the traditional owners of the Observatory site. Support for the operation of the MWA is provided by the Australian Government (NCRIS), under a contract to Curtin University administered by Astronomy Australia Limited. Establishment of the Murchison Radio-astronomy Observatory and the Pawsey Supercomputing Centre are initiatives of the Australian Government, with support from the Government of Western Australia and the Science and Industry Endowment Fund. We acknowledge the Pawsey Supercomputing Centre which is supported by the Western Australian and Australian Governments. Access to Pawsey Data Storage Services is governed by a Data Storage and Management Policy (DSMP). ASVO has received funding from the Australian Commonwealth Government through the National eResearch Collaboration Tools and Resources (NeCTAR) Project, the Australian National Data Service (ANDS), and the National Collaborative Research Infrastructure Strategy.

*Facilities:* *Chandra* (ACIS-S), ATCA, Blanco Telescope (DECAPS), *Gaia*, MeerKAT, MWA, SALT, VISTA (VVVX), VST (VPHAS+).

## REFERENCES

- Aguilera, D. N., Pons, J. A., & Miralles, J. A. 2008, *The Astrophysical Journal*, 673, L167, doi: [10.1086/527547](https://doi.org/10.1086/527547)
- Alonso-García, J., Saito, R. K., Hempel, M., et al. 2018, *A&A*, 619, A4, doi: [10.1051/0004-6361/201833432](https://doi.org/10.1051/0004-6361/201833432)
- Anzuini, F., Melatos, A., Dehman, C., Viganò, D., & Pons, J. A. 2022, *MNRAS*, 509, 2609, doi: [10.1093/mnras/stab3126](https://doi.org/10.1093/mnras/stab3126)
- Babusiaux, C., Fabricius, C., Khanna, S., et al. 2022, arXiv e-prints, arXiv:2206.05989. <https://arxiv.org/abs/2206.05989>
- Bailer-Jones, C. A. L., Rybizki, J., Fouesneau, M., Demleitner, M., & Andrae, R. 2021, *AJ*, 161, 147, doi: [10.3847/1538-3881/abd806](https://doi.org/10.3847/1538-3881/abd806)
- Briggs, D. S. 1995, in *Bulletin of the American Astronomical Society*, Vol. 27, American Astronomical Society Meeting Abstracts, 112.02
- Brinkworth, C. S., Burleigh, M. R., Lawrie, K., Marsh, T. R., & Knigge, C. 2013, *ApJ*, 773, 47, doi: [10.1088/0004-637X/773/1/47](https://doi.org/10.1088/0004-637X/773/1/47)
- Buckley, D. A. H., Swart, G. P., & Meiring, J. G. 2006, in *Society of Photo-Optical Instrumentation Engineers (SPIE) Conference Series*, Vol. 6267, Society of Photo-Optical Instrumentation Engineers (SPIE) Conference Series, ed. L. M. Stepp, 62670Z, doi: [10.1117/12.673750](https://doi.org/10.1117/12.673750)
- Buckley, D. A. H., Barnes, S. I., Burgh, E. B., et al. 2008, in *Society of Photo-Optical Instrumentation Engineers (SPIE) Conference Series*, Vol. 7014, Ground-based and Airborne Instrumentation for Astronomy II, ed. I. S. McLean & M. M. Casali, 701407, doi: [10.1117/12.789438](https://doi.org/10.1117/12.789438)
- Burgh, E. B., Nordsieck, K. H., Kobulnicky, H. A., et al. 2003, in *Society of Photo-Optical Instrumentation Engineers (SPIE) Conference Series*, Vol. 4841, Instrument Design and Performance for Optical/Infrared Ground-based Telescopes, ed. M. Iye & A. F. M. Moorwood, 1463–1471, doi: [10.1117/12.460312](https://doi.org/10.1117/12.460312)
- Caleb, M., Heywood, I., Rajwade, K., et al. 2022, *Nature Astronomy*, doi: [10.1038/s41550-022-01688-x](https://doi.org/10.1038/s41550-022-01688-x)
- Camilo, F., Ransom, S. M., Halpern, J. P., et al. 2006, *Nature*, 442, 892, doi: [10.1038/nature04986](https://doi.org/10.1038/nature04986)
- Camilo, F., Cognard, I., Ransom, S. M., et al. 2007, *ApJ*, 663, 497, doi: [10.1086/518226](https://doi.org/10.1086/518226)
- Cordes, J. M., Lazio, T. J. W., & McLaughlin, M. A. 2004, *NewAR*, 48, 1459, doi: [10.1016/j.newar.2004.09.038](https://doi.org/10.1016/j.newar.2004.09.038)
- Coti Zelati, F., Rea, N., Pons, J. A., Campana, S., & Esposito, P. 2018, *MNRAS*, 474, 961
- D’Ai, A., Evans, P. A., Gehrels, N., et al. 2016, *The Astronomer’s Telegram*, 9180, 1

- Deller, A. T., Camilo, F., Reynolds, J. E., & Halpern, J. P. 2012, *ApJL*, 748, L1, doi: [10.1088/2041-8205/748/1/L1](https://doi.org/10.1088/2041-8205/748/1/L1)
- Douchin, F., & Haensel, P. 2001, *A&A*, 380, 151, doi: [10.1051/0004-6361:20011402](https://doi.org/10.1051/0004-6361:20011402)
- Drew, J. E., Gonzalez-Solares, E., Greimel, R., et al. 2014, *MNRAS*, 440, 2036, doi: [10.1093/mnras/stu394](https://doi.org/10.1093/mnras/stu394)
- Erkut, M. H. 2022, *MNRAS*, 514, L41, doi: [10.1093/mnras/514/l41](https://doi.org/10.1093/mnras/514/l41)
- Esposito, P., Rea, N., & Israel, G. L. 2021, in *Astrophysics and Space Science Library*, Vol. 461, *Astrophysics and Space Science Library*, ed. T. M. Belloni, M. Méndez, & C. Zhang, 97–142, doi: [10.1007/978-3-662-62110-3\\_3](https://doi.org/10.1007/978-3-662-62110-3_3)
- Esposito, P., Rea, N., Borghese, A., et al. 2020, *ApJL*, 896, L30, doi: [10.3847/2041-8213/ab9742](https://doi.org/10.3847/2041-8213/ab9742)
- Ferrario, L., Wickramasinghe, D., & Kawka, A. 2020, *Advances in Space Research*, 66, 1025, doi: [10.1016/j.asr.2019.11.012](https://doi.org/10.1016/j.asr.2019.11.012)
- Fukugita, M., Ichikawa, T., Gunn, J. E., et al. 1996, *AJ*, 111, 1748, doi: [10.1086/117915](https://doi.org/10.1086/117915)
- Gaia Collaboration, Vallenari, A., & et al. 2022, *A&A*, in press
- Gaia Collaboration, Brown, A. G. A., Vallenari, A., et al. 2021, *A&A*, 649, A1, doi: [10.1051/0004-6361/202039657](https://doi.org/10.1051/0004-6361/202039657)
- Garmire, G. P., Bautz, M. W., Ford, P. G., Nousek, J. A., & Ricker, Jr., G. R. 2003, in *Proceedings of the SPIE.*, Vol. 4851, *X-Ray and Gamma-Ray Telescopes and Instruments for Astronomy.*, ed. J. E. Truemper & H. D. Tananbaum (SPIE, Bellingham), 28–44, doi: [10.1117/12.461599](https://doi.org/10.1117/12.461599)
- Gavriil, F. P., Gonzalez, M. E., Gotthelf, E. V., et al. 2008, *Science*, 319, 1802, doi: [10.1126/science.1153465](https://doi.org/10.1126/science.1153465)
- Gehrels, N. 1986, *ApJ*, 303, 336
- Geier, S., Raddi, R., Gentile Fusillo, N. P., & Marsh, T. R. 2019, *A&A*, 621, A38, doi: [10.1051/0004-6361/201834236](https://doi.org/10.1051/0004-6361/201834236)
- Gençali, A. A., Ertan, Ü., & Alpar, M. A. 2022, *MNRAS*, doi: [10.1093/mnras/514/l41](https://doi.org/10.1093/mnras/514/l41)
- Geng, J.-J., Zhang, B., & Huang, Y.-F. 2016, *ApJL*, 831, L10, doi: [10.3847/2041-8205/831/1/L10](https://doi.org/10.3847/2041-8205/831/1/L10)
- Gentile Fusillo, N. P., Tremblay, P. E., Cukanovaite, E., et al. 2021, *MNRAS*, 508, 3877, doi: [10.1093/mnras/stab2672](https://doi.org/10.1093/mnras/stab2672)
- González-Fernández, C., Hodgkin, S. T., Irwin, M. J., et al. 2018, *MNRAS*, 474, 5459, doi: [10.1093/mnras/stx3073](https://doi.org/10.1093/mnras/stx3073)
- Göğüş, E., Lin, L., Kaneko, Y., et al. 2016, *ApJL*, 829, L25, doi: [10.3847/2041-8205/829/2/L25](https://doi.org/10.3847/2041-8205/829/2/L25)
- Gudmundsson, E. H., Pethick, C. J., & Epstein, R. I. 1983, *ApJ*, 272, 286, doi: [10.1086/161292](https://doi.org/10.1086/161292)
- Han, J. L., Wang, C., Wang, P. F., et al. 2021, *Research in Astronomy and Astrophysics*, 21, 107, doi: [10.1088/1674-4527/21/5/107](https://doi.org/10.1088/1674-4527/21/5/107)
- He, C., Ng, C. Y., & Kaspi, V. M. 2013, *ApJ*, 768, 64, doi: [10.1088/0004-637X/768/1/64](https://doi.org/10.1088/0004-637X/768/1/64)
- Hewett, P. C., Warren, S. J., Leggett, S. K., & Hodgkin, S. T. 2006, *MNRAS*, 367, 454, doi: [10.1111/j.1365-2966.2005.09969.x](https://doi.org/10.1111/j.1365-2966.2005.09969.x)
- Hurley-Walker, N., Zhang, X., Bahramian, A., et al. 2022, *Nature*, 601, 526, doi: [10.1038/s41586-021-04272-x](https://doi.org/10.1038/s41586-021-04272-x)
- Hurley-Walker, N., Galvin, T. J., Duchesne, S. W., et al. 2022, *arXiv e-prints*, arXiv:2204.12762, <https://arxiv.org/abs/2204.12762>
- Jacoby, G. H., Hunter, D. A., & Christian, C. A. 1984, *ApJS*, 56, 257, doi: [10.1086/190983](https://doi.org/10.1086/190983)
- Kaspi, V. M., & Beloborodov, A. M. 2017, *ARA&A*, 55, 261, doi: [10.1146/annurev-astro-081915-023329](https://doi.org/10.1146/annurev-astro-081915-023329)
- Kawka, A., & Vennes, S. 2012, *A&A*, 538, A13, doi: [10.1051/0004-6361/201118210](https://doi.org/10.1051/0004-6361/201118210)
- Keane, E. F. 2018, *Nature Astronomy*, 2, 865, doi: [10.1038/s41550-018-0603-0](https://doi.org/10.1038/s41550-018-0603-0)
- Kilic, M., Kosakowski, A., Moss, A. G., Bergeron, P., & Conly, A. A. 2021, *ApJL*, 923, L6, doi: [10.3847/2041-8213/ac3b60](https://doi.org/10.3847/2041-8213/ac3b60)
- Loeb, A., & Maoz, D. 2022, *Research Notes of the American Astronomical Society*, 6, 27, doi: [10.3847/2515-5172/ac52f1](https://doi.org/10.3847/2515-5172/ac52f1)
- Lower, M. E., Shannon, R. M., Johnston, S., & Bailes, M. 2020, *ApJL*, 896, L37, doi: [10.3847/2041-8213/ab9898](https://doi.org/10.3847/2041-8213/ab9898)
- Lynch, R. S., Archibald, R. F., Kaspi, V. M., & Scholz, P. 2015, *ApJ*, 806, 266, doi: [10.1088/0004-637X/806/2/266](https://doi.org/10.1088/0004-637X/806/2/266)
- Lyne, A. G., Manchester, R. N., & Taylor, J. H. 1985, *MNRAS*, 213, 613, doi: [10.1093/mnras/213.3.613](https://doi.org/10.1093/mnras/213.3.613)
- Majid, W. A., Pearlman, A. B., Dobрева, T., et al. 2017, *ApJL*, 834, L2, doi: [10.3847/2041-8213/834/1/L2](https://doi.org/10.3847/2041-8213/834/1/L2)
- Manchester, R. N., Hobbs, G. B., Teoh, A., & Hobbs, M. 2005, *AJ*, 129, 1993, doi: [10.1086/428488](https://doi.org/10.1086/428488)
- Manchester, R. N., & Taylor, J. H. 1977, *Pulsars*
- Marsh, T. R., Gänsicke, B. T., Hümmelich, S., et al. 2016, *Nature*, 537, 374, doi: [10.1038/nature18620](https://doi.org/10.1038/nature18620)
- Minniti, D., Lucas, P. W., Emerson, J. P., et al. 2010, *NewA*, 15, 433, doi: [10.1016/j.newast.2009.12.002](https://doi.org/10.1016/j.newast.2009.12.002)
- Nimmo, K., Hessels, J. W. T., Kirsten, F., et al. 2022, *Nature Astronomy*, 6, 393, doi: [10.1038/s41550-021-01569-9](https://doi.org/10.1038/s41550-021-01569-9)
- O'Donoghue, D., Buckley, D. A. H., Balona, L. A., et al. 2006, *MNRAS*, 372, 151, doi: [10.1111/j.1365-2966.2006.10834.x](https://doi.org/10.1111/j.1365-2966.2006.10834.x)
- Offringa, A. R., McKinley, B., Hurley-Walker, N., et al. 2014, *MNRAS*, 444, 606, doi: [10.1093/mnras/stu1368](https://doi.org/10.1093/mnras/stu1368)
- Pearlman, A. B., Majid, W. A., Prince, T. A., Kocz, J., & Horiuchi, S. 2018, *ApJ*, 866, 160, doi: [10.3847/1538-4357/aade4d](https://doi.org/10.3847/1538-4357/aade4d)
- Pietka, M., Fender, R. P., & Keane, E. F. 2015, *MNRAS*, 446, 3687, doi: [10.1093/mnras/stu2335](https://doi.org/10.1093/mnras/stu2335)
- Pons, J. A., Miralles, J. A., & Geppert, U. 2009, *A&A*, 496, 207, doi: [10.1051/0004-6361:200811229](https://doi.org/10.1051/0004-6361:200811229)
- Potekhin, A. Y., Pons, J. A., & Page, D. 2015, *SSRv*, 191, 239, doi: [10.1007/s11214-015-0180-9](https://doi.org/10.1007/s11214-015-0180-9)
- Rea, N., Borghese, A., Esposito, P., et al. 2016, *ApJL*, 828, L13, doi: [10.3847/2041-8205/828/1/L13](https://doi.org/10.3847/2041-8205/828/1/L13)

- Rea, N., & Esposito, P. 2011, in *Astrophysics and Space Science Proceedings*, Vol. 21, High-Energy Emission from Pulsars and their Systems, 247, doi: [10.1007/978-3-642-17251-9\\_21](https://doi.org/10.1007/978-3-642-17251-9_21)
- Ronchi, M., Rea, N., Graber, V., & Hurley-Walker, N. 2022, arXiv e-prints, arXiv:2201.11704. <https://arxiv.org/abs/2201.11704>
- Sault, R. J., Teuben, P. J., & Wright, M. C. H. 1995, in *Astronomical Society of the Pacific Conference Series*, Vol. 77, *Astronomical Data Analysis Software and Systems IV*, ed. R. A. Shaw, H. E. Payne, & J. J. E. Hayes, 433. <https://arxiv.org/abs/astro-ph/0612759>
- Schlafly, E. F., & Finkbeiner, D. P. 2011, *ApJ*, 737, 103, doi: [10.1088/0004-637X/737/2/103](https://doi.org/10.1088/0004-637X/737/2/103)
- Schlafly, E. F., Green, G. M., Lang, D., et al. 2018, *ApJS*, 234, 39, doi: [10.3847/1538-4365/aaa3e2](https://doi.org/10.3847/1538-4365/aaa3e2)
- Schwab, J. 2021, *ApJ*, 906, 53, doi: [10.3847/1538-4357/abc87e](https://doi.org/10.3847/1538-4357/abc87e)
- Sokolowski, M., Colegate, T., Sutinjo, A. T., et al. 2017, *PASA*, 34, e062, doi: [10.1017/pasa.2017.54](https://doi.org/10.1017/pasa.2017.54)
- Straižys, V., & Lazauskaitė, R. 2009, *Baltic Astronomy*, 18, 19. <https://arxiv.org/abs/0907.2398>
- Tan, C. M., Bassa, C. G., Cooper, S., et al. 2018, *ApJ*, 866, 54, doi: [10.3847/1538-4357/aade88](https://doi.org/10.3847/1538-4357/aade88)
- Tingay, S. J., Goeke, R., Bowman, J. D., et al. 2013, *PASA*, 30, e007, doi: [10.1017/pasa.2012.007](https://doi.org/10.1017/pasa.2012.007)
- Tong, H. 2022, arXiv e-prints, arXiv:2204.01957. <https://arxiv.org/abs/2204.01957>
- Torres, S., Cantero, C., Rebassa-Mansergas, A., et al. 2019, *MNRAS*, 485, 5573, doi: [10.1093/mnras/stz814](https://doi.org/10.1093/mnras/stz814)
- Vasisht, G., & Gotthelf, E. V. 1997, *ApJL*, 486, L129+, doi: [10.1086/310843](https://doi.org/10.1086/310843)
- Vennes, S., Kawka, A., & Németh, P. 2011, *MNRAS*, 410, 2095, doi: [10.1111/j.1365-2966.2010.17584.x](https://doi.org/10.1111/j.1365-2966.2010.17584.x)
- Viganò, D., Garcia-Garcia, A., Pons, J. A., Dehman, C., & Graber, V. 2021, *Computer Physics Communications*, 265, 108001, doi: [10.1016/j.cpc.2021.108001](https://doi.org/10.1016/j.cpc.2021.108001)
- Viganò, D., Rea, N., Pons, J. A., et al. 2013, *MNRAS*, 434, 123, doi: [10.1093/mnras/stt1008](https://doi.org/10.1093/mnras/stt1008)
- Viganò, D., Pons, J., & Miralles, J. 2012, *Computer Physics Communications*, 183, 2042, doi: <https://doi.org/10.1016/j.cpc.2012.04.029>
- Wayth, R. B., Tingay, S. J., Trott, C. M., et al. 2018, *PASA*, 35, e033, doi: [10.1017/pasa.2018.37](https://doi.org/10.1017/pasa.2018.37)
- Weltevrede, P., Johnston, S., & Espinoza, C. M. 2011, *MNRAS*, 411, 1917, doi: [10.1111/j.1365-2966.2010.17821.x](https://doi.org/10.1111/j.1365-2966.2010.17821.x)
- Wilson, W. E., Ferris, R. H., Axtens, P., et al. 2011, *MNRAS*, 416, 832, doi: [10.1111/j.1365-2966.2011.19054.x](https://doi.org/10.1111/j.1365-2966.2011.19054.x)
- Yao, J. M., Manchester, R. N., & Wang, N. 2017, *ApJ*, 835, 29, doi: [10.3847/1538-4357/835/1/29](https://doi.org/10.3847/1538-4357/835/1/29)